



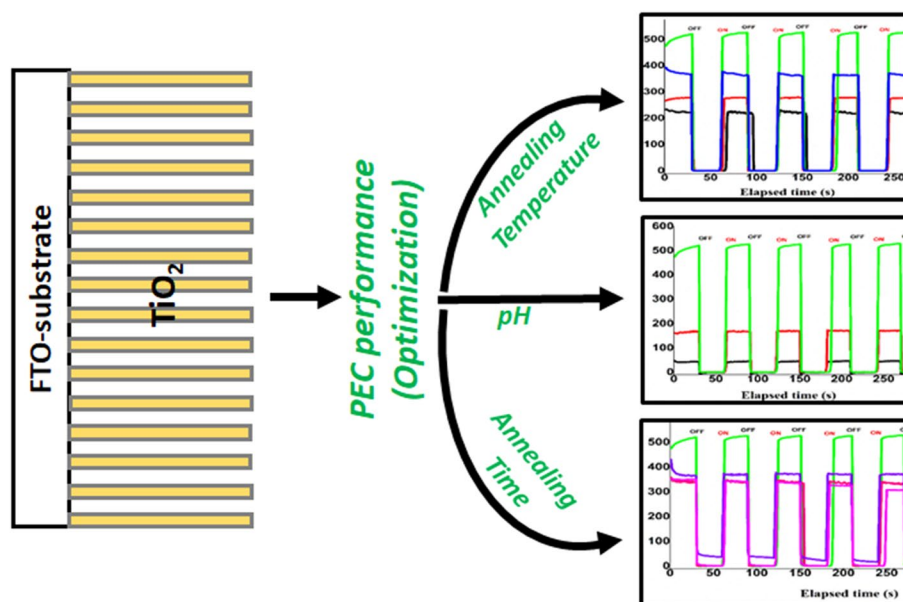
Optimization of conditions for improved solar energy harvesting application by hydrothermally grown TiO₂ nanorods

Muhammad Adil Mansoor^{1,2} · Farazila Binti Yusof¹ · Huang Nay-Ming³

Received: 30 September 2018 / Accepted: 31 December 2018 / Published online: 7 January 2019
© Iranian Chemical Society 2019

Abstract

In this study, using the optimum annealing temperature and time for hydrothermally grown TiO₂ nanorods, photooxidation of water at different pH values of the electrolyte solution is investigated. The composition, crystallinity and topographic studies of films, sintered at different temperatures of 200–500 °C for 2 h and annealed for 1–4 h at 400 °C, were evaluated by X-ray diffraction, Raman spectroscopy, X-ray photoelectron spectroscopy and field emission scanning electron microscopy. The sintering at high temperature and for longer time demonstrates an increase in crystallinity, but at the same time agglomeration of nanorods for prolonged heating and at high temperature leads to cracking at the surface of the films. Further, UV–Vis spectroscopic studies revealed prolonged heating and high-temperature sintering resulted in a red shift in light absorption edge of the films. The chronoamperometric measurement results under regular interrupted chopping revealed that the sample annealed at 400 °C for 2 h gives the best photoelectrochemical response with photocurrent density of 522 $\mu\text{A cm}^{-2}$ using 0.5M NaOH. The chronoamperometric response under different pH values of 13.7, 7.2 and 2.5 proved that TiO₂ gives the best response under a basic pH of 13.7 and the least under acidic media. The electrochemical impedance studies provided an insight into the charge transfer mechanism under dark and illumination with R_{ct} value of 1188.8 Ω under dark and 164.5 Ω under light conditions for the film annealed at 400 °C for 2 h.



Electronic supplementary material The online version of this article (<https://doi.org/10.1007/s13738-018-01586-y>) contains supplementary material, which is available to authorized users.

Extended author information available on the last page of the article

Keywords TiO₂ nanorods · Surface morphology · Optical band gap · Photocurrent density

Introduction

Photoelectrocatalysis has the potential to facilitate the consumption of natural sunlight, a clean and energy-rich source, for the purpose of environmental remediation (pollutant degradation) and clean energy production [1–3]. Due to significant practical interest, intensive research efforts to develop novel photocatalyst materials to improve the photoelectrochemical efficiency, in particular under visible/solar illumination, have been intensified worldwide. Since the first study of photoelectrochemical (PEC) water splitting on TiO₂ by Fujishima and Honda in 1972 [4], lot of efforts have been taken to synthesize photoelectrodes for better solar-to-hydrogen conversion efficiency. Among several photoactive materials with their own pros and cons, TiO₂ has been investigated extensively due to its photocorrosion-resistive properties, non-toxicity, stability and low cost [5–9]. However, low quantum yield and high band gap (3.3 eV) are the key factors that hinder its photoelectrochemical water splitting efficiency [10, 11]. Earlier efforts were focused on developing nanoparticles of TiO₂ to enhance surface area for better light-harvesting efficiency. But the charge recombination and least electron mobility at the grain boundary could not help in achieving superior water splitting efficiency. Recently, a new approach of developing one-dimensional (1D) nanostructures, such as nanotubes, nanorods and nanowires, has been introduced. As compared to planar TiO₂ films, this new approach of developing 1D structures engenders more surface area and thus provides improved charge transportation (high mobility), charge separation (least recombination) and smaller diffusion distance of carriers [12–15].

Several fabrication processes have been developed for the synthesis of 1D TiO₂ nanorods, nanowires, or nanotubes, such as colloidal synthesis [16, 17], electrodeposition [18], organometallic chemical vapour deposition (OMCVD) [19, 20], chemical vapour deposition (CVD) [21, 22], oblique-angle deposition (OAD) [23] and hydrothermal processes [24, 26–26]. Among these, the hydrothermal synthesis of rutile TiO₂ has certain advantages, such as the product is synthesized at low-temperature conditions that mitigate the chance of agglomeration [27]; secondly, by changing certain the reaction conditions, the morphology and topography of the product can be altered. Moreover, the product has high purity due to recrystallization in hydrothermal solution. Further to enhance crystallinity, the product can be subjected to mild annealing at different temperatures [28]. In the past few years, many researchers have reported the formation of one-dimensional TiO₂ [29, 30], including TiO₂ hybrid structures with other ceramic materials using 1D TiO₂ as template [31]. But different researchers used different conditions such as

annealing temperature, annealing time and pH of the electrolyte. It is hard to find any work regarding optimization of these conditions for superior photocatalytic efficiency prior to use of these films in pure form as well as for the production of hybrid materials. It is well reported that the annealing temperature and time have a direct impact on the morphology and interconnection of grains in the metal oxide matrix [32, 33]. Similarly, the pH of the electrolyte plays a vital role in the interaction of the electrolyte with photo-generated holes [34].

In the present work, efforts are made to optimize the different conditions such annealing temperature and time for the growth of hydrothermally prepared 1D TiO₂ nanorods. In this effort, films after synthesis at different temperatures and for different annealing times were subjected to their complete characterization by using different techniques such as XRD, XPS, FE–SEM, Raman spectroscopy, photoluminescence and UV–Vis spectroscopy. Later, the photoelectrochemical behaviour of these films was studied under different pH values of the electrolyte to get the best results for their photoelectrocatalytic behaviour.

Materials and methods

Synthesis of TiO₂ nanorods

The TiO₂ nanorods were grown on FTO (fluorine-doped tin oxide) substrate using the reported hydrothermal synthesis method [30]. In a typical reaction, 15 mL of hydrochloric acid (HCl; 36 wt%) was added to 15 mL of deionized (DI) water in a 100 mL beaker. After stirring for a few minutes, 0.5 mL titanium *n*-butoxide was added in a stirring mixture. The mixture was allowed to stir at room temperature for about 2 h and the clear solution was transferred to a Teflon-lined stainless steel autoclave (50 mL volume), where the FTO substrate was submerged in the solution. The sealed autoclave was heated in an electric oven at 165 °C for 8 h, followed by slow cooling to room temperature. The white mass of as-grown TiO₂ nanorods on the FTO substrate was then washed thoroughly with deionized water and dried under air. Following the same procedure, seven different films on FTO were synthesized to evaluate the effect of temperature and annealing time. Four of these seven films were annealed at 200, 300, 400 and 500 °C for 2 h and the remaining three were sintered at 400 °C for 1, 3 and 4 h (s) to increase the crystallinity of TiO₂ nanorods and improve their contact to the substrate. The coding assigned to these seven samples is available in ESI as Table S1.

Characterization of photoanode

The crystalline phase of the samples was determined by X-ray powder diffraction (XRD) on a D8 Advance X-Ray Diffractometer-Bruker AXS using Cu-K α radiation ($\lambda = 1.542 \text{ \AA}$), at a voltage of 40 kV and current of 40 mA at ambient temperature. X-ray photoelectron spectroscopy (XPS) measurements were performed using ULVAC-PHI Quantera II (Ulvac-PHI, INC.) with monochromatic Al-K α ($h\nu = 1486.6 \text{ eV}$) operating at 25.6 W (beam diameter of 100 μm) X-ray source and pass energy of 112 eV with 0.1 eV per step for narrow scan analysis. Raman spectroscopy was carried out using a RENISHAW, INVIA, WiRE 3.4 (with 514 nm Ar laser) Raman Spectrophotometer. The spectrum was recorded in the range of 100–1000 cm^{-1} . The topography of as-grown thin films was studied by a field-emission gun scanning electron microscope (FESEM, FEI Quanta 400) coupled with energy-dispersive X-ray (EDX) spectrometer INCA Energy 200 (Oxford Inst.), at an accelerating voltage of 20 kV, 10,000 magnification and a working distance of 9 mm. The optical absorption properties of the thin films were recorded on Lambda 35 Perkin-Elmer UV-Vis spectrophotometer in the spectral region of 300–900 nm using similar FTO-coated glass substrate as a reference to eliminate the substrate impact in the spectrum. The photoelectrochemical properties of TiO $_2$ electrodes were measured using a standard three-electrode electrochemical cell fitted with a quartz window. Ag/AgCl/3M KCl and Pt electrodes were employed as the reference and counter electrodes, respectively, and the measurements were carried out in 0.5 M NaOH aqueous electrolyte. A 150-W Xenon Arc Lamp (Newport, Model 69907) containing a simulated AM 1.5 G filter was used as a light source throughout the experiments. The chronoamperometric and electrochemical impedance spectroscopic (EIS) measurements were recorded by a computer-controlled VersaSTAT 3 electrochemical workstation (Princeton Applied Research, USA), using a standard three-electrode electrochemical cell fitted with a quartz window. Ag/AgCl electrode and Pt were employed as the reference and counter electrodes, respectively, and all the measurements were carried out in 0.5 M NaOH aqueous electrolyte. The cells were illuminated by a 150-W Xenon Arc Lamp (Newport, Model 69907) containing a simulated AM 1.5 G filter at 100 mW cm^{-2} light intensity. The effective area of the film was adjusted to 1 \times 1 cm^2 .

Results and discussions

Structural analysis

The X-ray spectra of all the samples annealed under different conditions (Fig. 1a, b) specify that the relative intensities

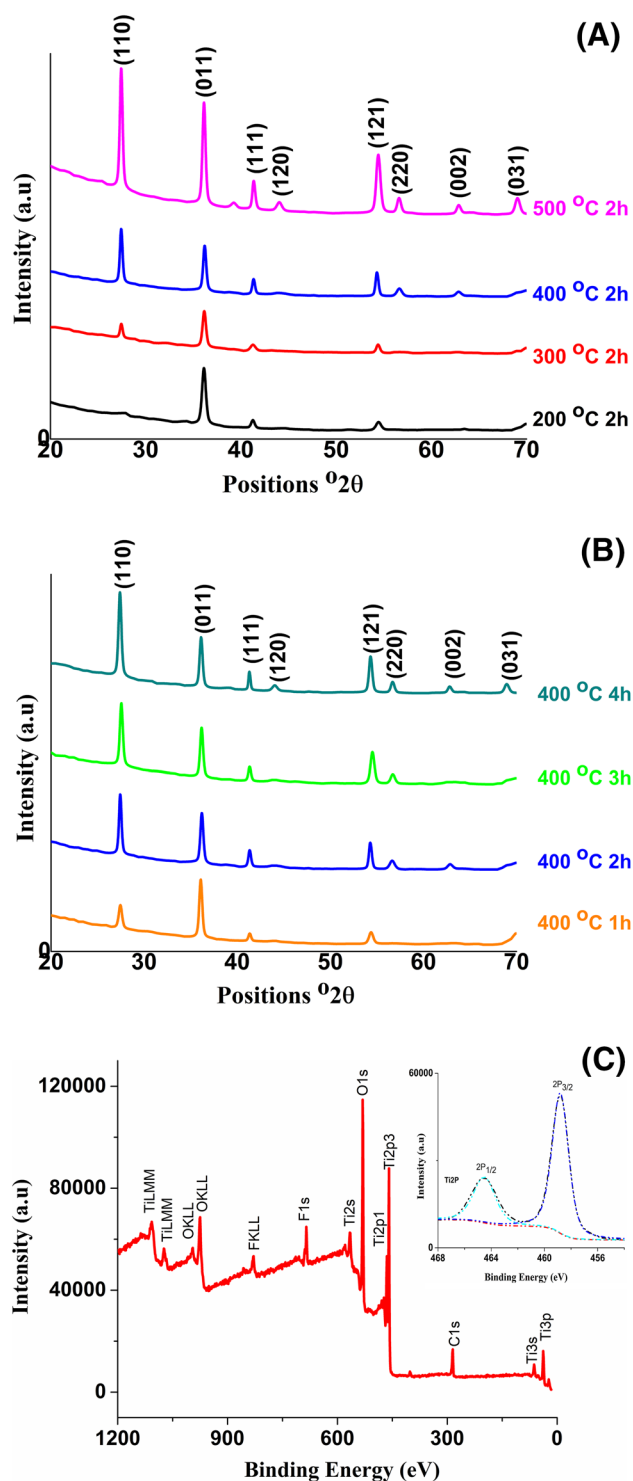


Fig. 1 The X-ray diffraction pattern of TiO $_2$ nanorods annealed at **a** 200–500 °C for 2 h and **b** 400 °C for 1–4 h, while **c** represent the XPS survey scan with an inset of narrow scan for Ti 2p

and the reflection positions agree well with the standard COD card No. [96-900-4142] for rutile TiO $_2$. This TiO $_2$ (rutile) exhibits a tetragonal crystal system with cell parameters of $a = 4.59$ and $c = 2.95 \text{ \AA}$. The corresponding reflections at

2θ values of 27.44° , 36.08° , 41.24° , 44.05° , 54.32° , 56.63° , 62.75° and 69.01° are related to (110), (011), (111), (120), (121), (220), (002) and (031) lattice reflection planes of a $\text{TiO}_{2(\text{rutile})}$, respectively. However no extra peak for any other phase of TiO_2 appeared. Stick pattern matching with standard is available in Fig. S1 in supplementary data.

The variation in the diffraction peak intensity of TiO_2 nanorods, in the 2θ region of 27.4 , is analyzed for films annealed at different temperatures (200–500 °C or 2 h) and time of 1–4 h at 400 °C as shown in Fig. 1a, b. The diffraction peak becomes more intensified with annealing at high temperature as well as for prolonged annealing at constant temperature, indicative of most enhanced crystallinity and grain growth [35, 36]. It is observed that at 200 and 300 °C, the peak for the (110) plane is not much intense, but as soon as the temperature goes to 400 °C the crystal growth along the (110) direction proceeds and as a result the peak for the (110) plane gets intensified at elevated temperature and for prolonged heating, in accordance with the rutile phase of TiO_2 produced at high temperatures [32, 37].

The XPS spectrum (shown in Fig. 1c) of the TiO_2 nanorod annealed at 400 °C for 2 h was recorded to analyze and determine the chemical composition and identify the chemical states of Ti. The inset of Fig. 1c shows the Ti 2p spectrum in which two peaks are observed at 458.7 and 464.5 eV, corresponding to the binding energies of $\text{Ti}2p_{3/2}$ and $\text{Ti}2p_{1/2}$ core levels due to the presence of the Ti(IV) state [38].

The Raman spectra of TiO_2 nanorods (Fig. 2a, b) recorded in the region of $100\text{--}1000\text{ cm}^{-1}$ divulge four distinct Raman peaks at 142.7 (weak), 235.3 (weak), 449.3 (strong) and 609.9 cm^{-1} (strong) that correspond to B_{1g} , second-order scattering, E_g and A_{1g} scattering modes, respectively. These peaks represented the O–Ti–O bending-type vibrations and the Ti–O bond stretching-type vibrations. The peak positions are in good agreement with the rutile phase of TiO_2 [39]. By comparing the peak at 447 cm^{-1} (E_g) of samples calcined at different temperatures and times, it is clear that the relative intensity of the peak increases with increase in sintering temperature as well as for increased heating time. It is reported that prolonged calcination and high temperature not only improve crystallinity, but also reduce the surface area of nanoparticles. These changes directly impart effect on the full-width half maxima (FWHM) and the intensity of peaks in the Raman spectra [40]. From the present results, it is revealed that FWHM is decreased with increase in annealing time and temperature (Fig. 2c). The FWHM values for the peak at 447 cm^{-1} (E_g) are shown in Table 1.

Morphological studies

Figure 3a–d shows the FESEM images of TiO_2 nanorods annealed at different temperatures of 200, 300, 400 and

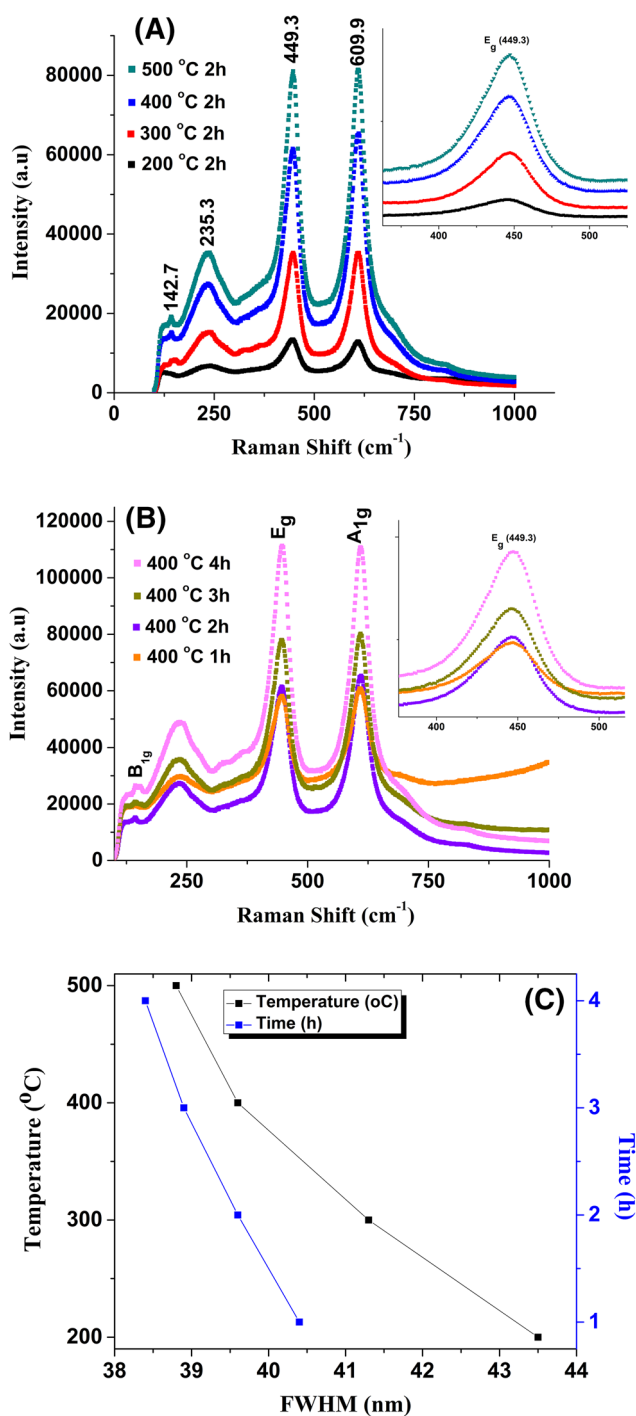


Fig. 2 Raman spectra of rutile TiO_2 nanorods annealed at different temperatures (200–500 °C for 2 h) (a) and for different sintering times of 1–4 h at 400 °C (b), while c represents the variation in FWHM with change in annealing temperature (black) and time (blue)

500 °C for 2 h and different annealing times of 1, 2, 3 and 4 h at 400 °C, respectively. The FESEM results show that highly ordered TiO_2 nanorods in the form of columns are grown perpendicularly from the surface of the FTO substrate

Table 1 FWHM values of samples annealed at different temperatures and times with Raman spectrum peak at 449.3 cm^{-1}

Samples annealed at different temperature for 2 h		FWHM (nm)	Samples annealed for different time at 400 °C		FWHM (nm)
Temperature (°C)	Code		Time (h)	Code	
200	200 2 h	43.5	1	400 1 h	40.4
300	300 2 h	41.3	2	400 2 h	39.6
400	400 2 h	39.6	3	400 3 h	38.9
500	500 2 h	38.8	4	400 4 h	38.4

in all the samples. Each column seems to comprise a number of nanorods with average diameter of 25–110 nm and a vertical length of 3–3.5 μm (ESI Figs. S2 and S3). Further it is observed that with increment in annealing temperature (200–500 °C), cracking and agglomeration start, but the dimensions of the nanorods remain unaffected. Topographical studies reveal that the cracking becomes more intense as we go to high annealing temperature; however, the edge of top of rod becomes sharp (ESI Fig. S2). Cracks may result from the thermal stresses at higher temperature and increase in particle size due to agglomeration that is evident for high-temperature annealing [32, 36, 41, 42]. Similarly, at 400 °C (Fig. 3e–h), change in the annealing time (1–4 h) provides the same observations. These observations tend to speculate that elevated temperature and prolonged heating result in more cracks.

Optical band gap

Figure 4a and b shows the UV–visible absorbance spectra of TiO_2 nanorods annealed at 200–500 °C for 2 h and at 400 °C for 1–4 h, respectively. The spectra were recorded in wavelength range of 300–900 nm. It is noticed that the samples show an absorption edge around 410 nm that gives a slight redshift as the annealing temperature and time are increased. A systematic redshift with increase in annealing time and temperature is clearly visible in insets of Fig. 4a, b. It is evidenced that with increase in temperature, crystallinity increases that leads to absorption at higher wavelength. Ultimately, the redshift due to more crystallinity and larger grain size results in the reduction of the optical direct band gap [40].

The direct band gap values of samples annealed at different temperatures and times were estimated by using the following Tauc's equation [43, 44]:

$$\alpha h\nu = A(h\nu - E_g)^\gamma, \quad (1)$$

where α is the linear absorption coefficient of the material, $h\nu$ is the photon energy, A is a proportionality constant and

γ is a constant depending on the band-gap nature; $\gamma = 1/2$ for allowed direct band gap and $\gamma = 2$ for indirect band gap. For a direct band gap, the Tauc equation can be rearranged as $(\alpha h\nu)^\gamma = A_1(h\nu - E_g)$. A plot of $(\alpha h\nu)^\gamma$ versus $h\nu$ would have a linear region with slope A_1 and whose extrapolation to $\alpha(h\nu) = 0$ would give the value of direct band gap. The values of direct band gaps extracted from Fig. 4c, d are shown in Table 2. The trend of direct band gap with increasing temperature and prolonged heating is shown in Fig. 5. The results reveal that high temperature and prolonged heating give rise to redshift and reduced band gap.

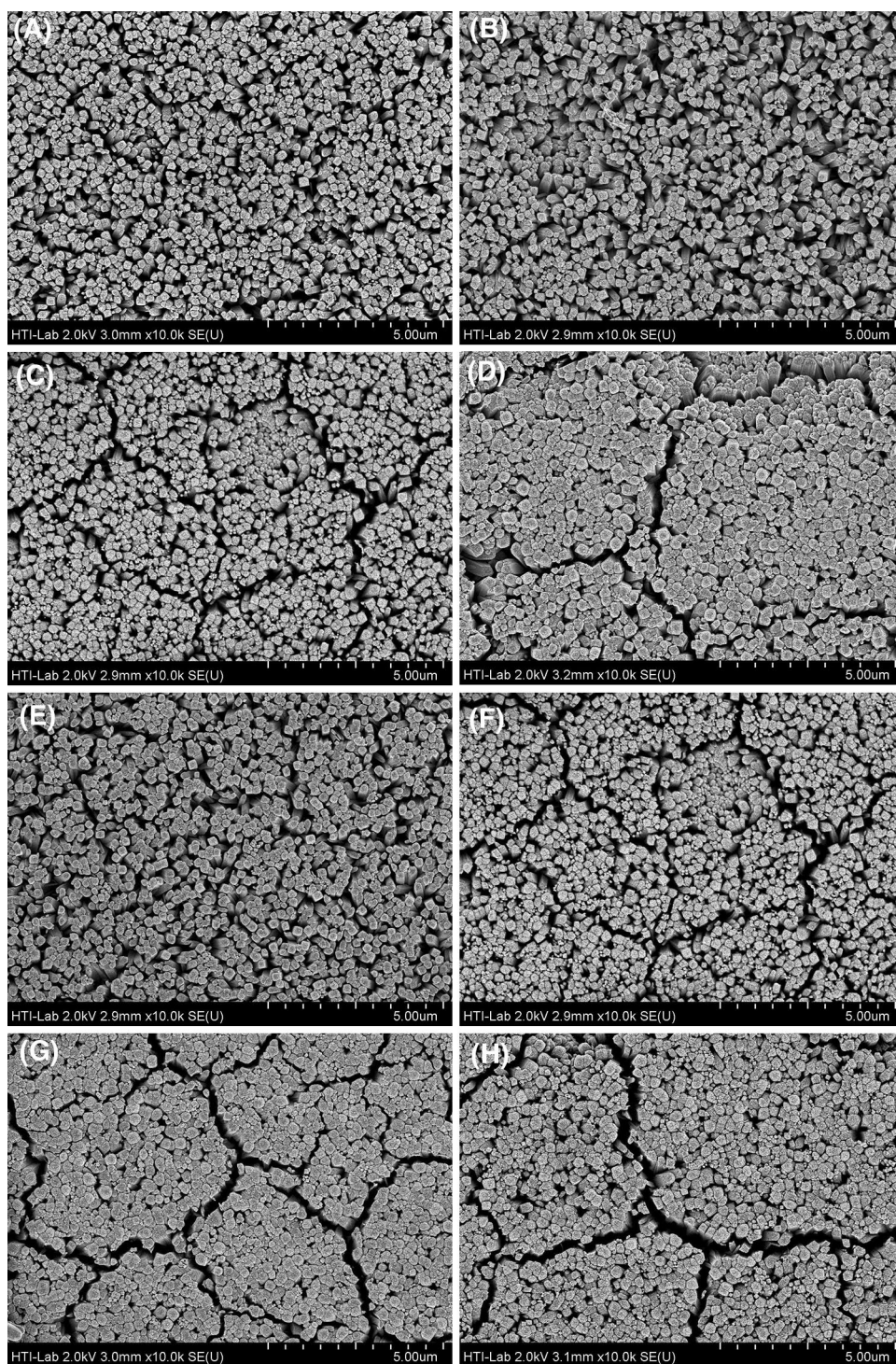
Photoelectrochemical response

To scrutinize the influence of change in morphology on photocatalysis of water, the photoelectrochemical response of TiO_2 photoanodes annealed at different temperatures and times was measured in 0.5M NaOH under 1 sun illumination while regularly interrupted by chopping. Figure 6a, b represents the plots of photocurrent density (J) against elapsed time (t). It is observed that while increasing annealing temperature from 200 to 400 °C, there is a gradual increase in photocurrent density from 217 to 522 $\mu\text{A cm}^{-2}$, but a noticeable decrease in photocurrent is observed when the temperature rises to 500 °C, where it gives a photocurrent density of 368 $\mu\text{A cm}^{-2}$. Similarly for the films annealed at 400 °C for 1–4 h, it is found that prolonged annealing for 3 and 4 h shows low value of photocurrent density than the sample annealed for 2 h. The stability of electrodes in terms of photocurrent density at elapsed time of 30 s and 270 s is provided in Table 3 (Fig. S3 in ESI).

It is evident that heating improves crystallinity that facilitates better electron transport with least e^- – h^+ recombination. Herein, we find that with increasing temperature or prolonged heating, there is a sharp increase in photocurrent density up to a certain optimum condition, after which despite better crystallinity there is reduction in photocurrent density [33, 45]. It is believed that extensive heat either as high temperature or for longer time results in agglomeration with cracked surface (Fig. 3). This cracking and coalescence increase the surface barrier layers, stress and defects, reduction in surface area, and ultimately longer distance for holes to travel and hence much of the photogenerated carriers recombine. Moreover, coalescence hinders most of the active part (reduction in surface area) from interacting with the electrolyte.

The further effect of pH by using electrolytes at three different pH values (13.7, 7.2 and 2.5) is also inspected. A pH of 13.7 was maintained by using 0.5M NaOH as an electrolyte, while phosphate buffer saline (PBS) was used to attain pH of 2.5 and 7.2. Figure 7 shows the chronoamperometric measurements recorded for the samples annealed at 400 °C for 2 h, which give an appreciable photocurrent density of

Fig. 3 FESEM images of TiO₂ nanorods annealed at 200, 300, 400 and 500 °C for 2 h (a–d) and at 400 °C for 1 h (e–f)



522 $\mu\text{A cm}^{-2}$ at basic pH of 13.7. But this photoresponse declines drastically as we go from basic to neutral media ($J = 170.6 \mu\text{A cm}^{-2}$) and further decreases in acid media ($J = 47.2 \mu\text{A cm}^{-2}$). Similar results have been reported that reveal by changing the pH from 13 to 10, about four times the photoresponse was reduced and photocurrent density declined further, when it was shifted to acidic pH. To explain

the effect of pH on photocatalysis of water by TiO₂(rutile) electrode, two different pathways have been suggest by Samuel et al. [34]. The plausible mechanism is designed with electrode–electrolyte interaction at the surface of the electrodes. In the first possible pathway, H₂O adsorbs on the surface of the electrode and interacts with photo-generated holes to produce a proton (H⁺) and hydroxyl radical (OH[•]).

Fig. 4 The UV–Vis absorbance spectra of films annealed **a** at 200–500 °C for 2 h and **b** for 1–4 h at 400 °C. **c, d** The optical band gaps for the films annealed at different temperatures and times, respectively

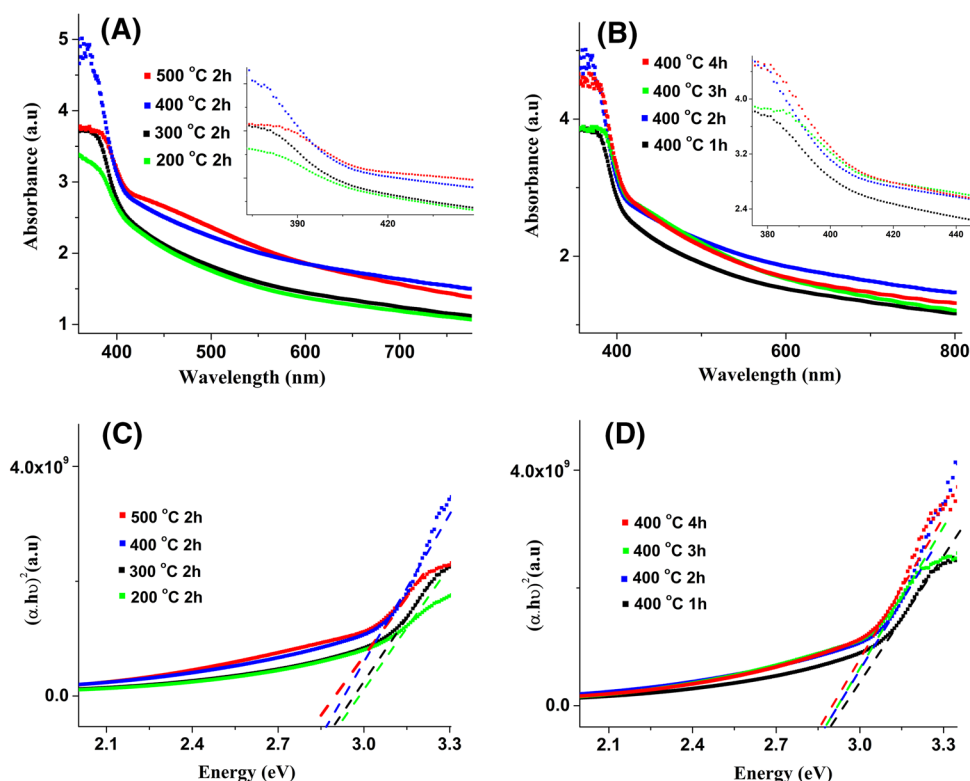


Table 2 Direct band gaps of TiO₂ nanorod at different annealing temperatures and times

Samples annealed at different temperatures for 2 h		Direct band gap (eV)	Samples annealed for different times at 400 °C		Direct band gap (eV)
Temperature (°C)	Code		Time (h)	Code	
200	200 2 h	2.91	1	400 1 h	2.90
300	300 2 h	2.89	2	400 2 h	2.86
400	400 2 h	2.86	3	400 3 h	2.86
500	500 2 h	2.82	4	400 4 h	2.85

In the next step, hydroxyl radicals produce water and oxygen. In the second suggested pathway, hydroxyl ions adsorb on the surface of electrode and oxidize to hydroxyl radical, followed by the production of water and oxygen in the next step. These two plausible pathways of electrolyte interaction at the surface of the electrode are available in supplementary data. It is noted that both the mechanisms are quite identical except for the adsorbed species, that is, water in the first possible pathway, while hydroxyl ions are adsorbed in the second possibility. It is observed that the photocurrent density enhances abruptly when the pH of the electrolyte is increased. This might be due to increase in the number of sites occupied by hydroxyl ions which rapidly interact with holes. Therefore hydroxyl ions release oxygen quicker than

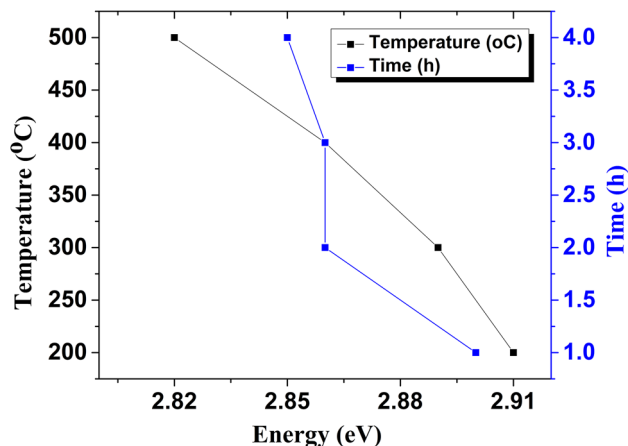


Fig. 5 The drift in optical band gap values with respect to annealing temperature (black) and sintering time (blue)

water and increase the current density. The best explanation is that the negatively charged species interacts rapidly with the positively charged photogenerated hole than neutral species (H₂O). The reduction in the current at neutral and acidic pH is considered due lack of negative ions and thus the first possibility of water adsorption dominates at lower pH values.

Additionally, electrochemical impedance (EIS) studies of sample annealed at 400 °C for 2 h were also performed to evaluate the charge transfer and recombination phenomenon

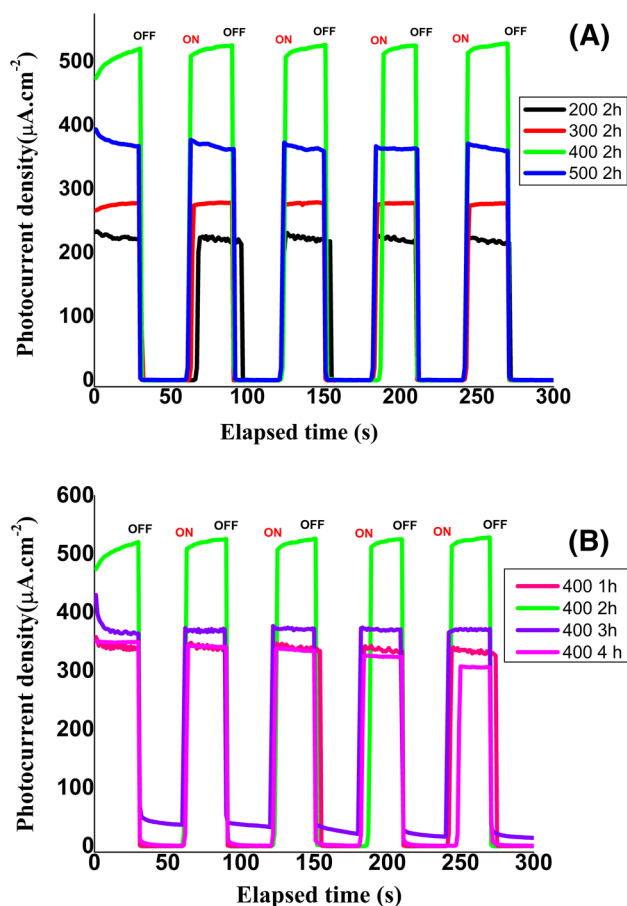


Fig. 6 Chronoamperometric measurements of rutile TiO_2 nanorods annealed at **a** 200–500 °C for 2 h and **b** 400 °C for 1–4 h

in dark and light conditions using 0.5M NaOH in the range of 0.01 Hz–0 K Hz. Figure 8 shows the experimental and fitted (insets) Nyquist plot under light and dark conditions. The experimental results show formation of a bigger semi-circle under dark conditions. The formation of larger diameter of the extrapolated circle under dark conditions shows the deterrence of electron transfer kinetics at the surface of the photoanode, while the formation of a small semicircle demonstrates more convenience in electron transport with least charge recombination under light conditions. The R_{ct}

value of TiO_2 film annealed at 400 °C for 2 h decreases significantly from 1188.8 Ω to 162.4 Ω after light illumination, indicating an increase in the charge carriers and reducing the possibility of the charge recombination, and thus enhancing the photocurrent response against water oxidation.

Conclusion

The present studies have been performed to optimize the best conditions for the synthesis of TiO_2 nanorods for its improved light-harvesting efficiency. For this purpose, hydrothermally produced TiO_2 nanorods were subjected to different annealing temperatures (200–500 °C) as well as different annealing times at 400 °C. The XRD and Raman spectroscopic studies divulge that the crystallinity of the samples is improved as the annealing temperature and time is increased. At the same time, FESEM images explicate that the agglomeration and cracking increase at high temperatures and for prolonged heating. Moreover, the agglomeration tends to reduce the optical band gap of as-grown films. Finally, the photoelectrochemical response in terms of chronoamperometry revealed that the sample annealed at 400 °C for 2 h gives the best photoresponse. The samples annealed below 400 °C and at 400 °C for 1 h show poor response due to lack of certain crystallinity, while the drop of photoresponse in the samples annealed at 500 °C for 2 h and 400 °C for 3 and 4 h is due to reduced surface area. Further, estimation of the effect of the pH of the electrolyte on the photoresponse of the film grown at 400 °C for 2 h exposed that the photoactivity of TiO_2 nanorods is directly related to OH^- ion concentration and gives the best value of 522 $\mu\text{A cm}^{-2}$ at pH of 13.7 using 0.5M NaOH. The electrochemical impedance studies aided in understanding the charge transfer mechanism under dark and illumination. It is found that R_{ct} value of 1188.8 Ω under dark reduced to 164.5 Ω under light conditions. We believe these optimized conditions will help researchers working in the field of photoelectrochemical water splitting, especially those endeavouring in the design of hybrid TiO_2 nanorods.

Table 3 Variation in photocurrent density with annealing temperature and time

Samples annealed at different temperatures for 2 h		Photocurrent density ($\mu\text{A cm}^{-2}$)		Samples annealed for different times at 400 °C		Photocurrent density ($\mu\text{A cm}^{-2}$)	
Temperature (°C)	Code	At 30 s	At 270 s	Time (h)	Code	At 30 s	At 270 s
200	200 2 h	217	216	1	400 1 h	349	325
300	300 2 h	277	277	2	400 2 h	522	528
400	400 2 h	522	528	3	400 3 h	362	368
500	500 2 h	368	355	4	400 4 h	343	306

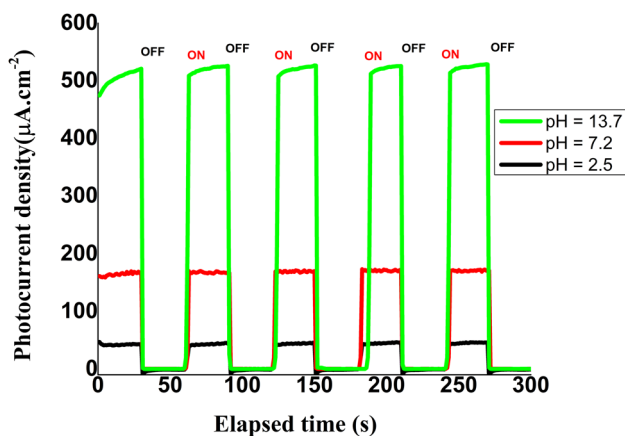


Fig. 7 Photoelectrochemical response of TiO₂ nanorods (400 °C 2 h) under different electrolyte pH values of 13.7, 7.2 and 2.5

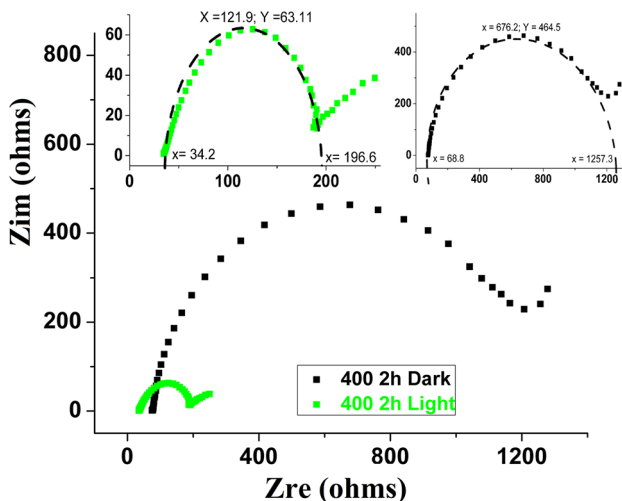


Fig. 8 Electrochemical impedance plot showing the experimental and fitted (insets) impedance data under light and dark conditions for the films of TiO₂ nanorods annealed at 400 °C for 2 h

Funding This study was funded by the FRGS Grant No. FP062-2015A.

Compliance with ethical standards

Conflict of interest The authors declare that there is no conflict of interest.


References

1. D. Pile, *Nat Photon* **6**, 637 (2012)
2. A. Paracchino, V. Laporte, K. Sivula, M. Grätzel, E. Thimsen, *Nat. Mater.* **10**, 456 (2011)
3. J.C. Grenier, J.M. Bassat, F. Mauvy, in *Functional materials for sustainable energy applications*, eds. by J. A. Kilner, S.J. Skinner,

- S.J.C. Irvine, P.P. Edwards (Woodhead Publishing, Sawston, 2012), p. 402 <https://doi.org/10.1533/9780857096371.3.402>
4. A. Fujishima, K. Honda, *Nature* **238**, 37 (1972)
5. O. Carp, C.L. Huisman, A. Reller, *Prog. Solid State Chem.* **32**, 33 (2004)
6. J.H. Park, S. Kim, A.J. Bard, *Nano Lett.* **6**, 24 (2006)
7. M. Ksibi, S. Rossignol, J.-M. Tatibouët, C. Trapalis, *Mater. Lett.* **62**, 4204 (2008)
8. J. Yu, L. Qi, M. Jaroniec, *J. Phys. Chem. C* **114**, 13118 (2010)
9. S. Liu, J. Yu, M. Jaroniec, *Chem. Mater.* **23**, 4085 (2011)
10. M.G.I.N. Murdoch, G.I.N. Waterhouse, M.A. Nadeem, J.B. Metson, M.S. Keane, R.F. Howe, J. Llorca, H. Idriss, *Nat. Chem.* **3**, 489 (2011)
11. J. Yu, J. Ran, *Energy Environ. Sci.* **4**, 1364 (2011)
12. D. Zhang, M. Wen, S. Zhang, P. Liu, W. Zhu, G. Li, H. Li, *Appl. Catal. B* **147**, 610 (2014)
13. J. Bian, C. Huang, L. Wang, T. Hung, W.A. Daoud, R. Zhang, *ACS Appl. Mater. Interfaces.* **6**, 4883 (2014)
14. Q. Zhou, S. Zhang, X. Yang, Q. Wu, H. Zhao, M. Wu, *Sens. Actuators B* **186**, 132 (2013)
15. Q. Mu, Y. Li, Q. Zhang, H. Wang, *J. Hazard. Mater.* **188**, 363 (2011)
16. E.C. Scher, L. Manna, A.P. Alivisatos, *Philos. Trans. R. Soc. Lond. Ser. A: Math. Phys. Eng. Sci.* **361**, 241 (2003)
17. L. Manna, E.C. Scher, A.P. Alivisatos, *J. Am. Chem. Soc.* **122**, 12700 (2000)
18. X.Y. Zhang, L.D. Zhang, W. Chen, G.W. Meng, M.J. Zheng, L.X. Zhao, F. Philipp, *Chem. Mater.* **13**, 2511 (2001)
19. Y. Li, J. Xiang, F. Qian, S. Gradečak, Y. Wu, H. Yan, D.A. Blom, C.M. Lieber, *Nano Lett.* **6**, 1468 (2006)
20. S. Gradečak, F. Qian, Y. Li, H.-G. Park, C.M. Lieber, *Appl. Phys. Lett.* **87**, 173111 (2005)
21. T. Kuykendall, P. Ulrich, S. Aloni, P. Yang, *Nat. Mater.* **6**, 951 (2007)
22. D.A. Boyd, L. Greengard, M. Brongersma, M.Y. El-Naggar, D.G. Goodwin, *Nano Lett.* **6**, 2592 (2006)
23. A. Wolcott, W.A. Smith, T.R. Kuykendall, Y. Zhao, J.Z. Zhang, *Small* **5**, 104 (2009)
24. L. Vayssieres, *Adv. Mater.* **15**, 464 (2003)
25. L. Vayssieres, K. Keis, S.-E. Lindquist, A. Hagfeldt, *J. Phys. Chem. B* **105**, 3350 (2001)
26. B. Liu, E.S. Aydil, *J. Am. Chem. Soc.* **131**, 3985 (2009)
27. H. Cheng, J. Ma, Z. Zhao, L. Qi, *Chem. Mater.* **7**, 663 (1995)
28. Z. Yang, B. Wang, H. Cui, H. An, Y. Pan, J. Zhai, *J. Phys. Chem. C* **119**, 16905 (2015)
29. Y.-C. Pu, Y. Ling, K.-D. Chang, C.-M. Liu, J.Z. Zhang, Y.-J. Hsu, Y. Li, *J. Phys. Chem. C* **118**, 15086 (2014)
30. G. Wang, H. Wang, Y. Ling, Y. Tang, X. Yang, R.C. Fitzmorris, C. Wang, J.Z. Zhang, Y. Li, *Nano Lett.* **11**, 3026 (2011)
31. Y. Li, S. Ji, Y. Gao, H. Luo, M. Kanehira, *Sci. Rep.* **3**, 1370 (2013)
32. Y. Sun, K. Yan, G. Wang, W. Guo, T. Ma, *J. Phys. Chem. C* **115**, 12844 (2011)
33. M. Rozana, K. Abdul Razak, C.K. Yew, Z. Lockman, G. Kawamura, A. Matsuda, *J. Mater. Res.* **31**, 1681 (2016)
34. S. Crawford, E. Thimsen, P. Biswas, *J. Electrochem. Soc.* **156**, H346 (2009)
35. N.R. Mathews, E.R. Morales, M.A. Cortés-Jacome, J.A. Toledo, Antonio, *Sol. Energy* **83**, 1499 (2009)
36. D. Zhao, T. Peng, L. Lu, P. Cai, P. Jiang, Z. Bian, *J. Phys. Chem. C* **112**, 8486 (2008)
37. A.K.M. Muaz, U. Hashim, F. Ibrahim, K.L. Thong, M.S. Mohhtar, W.-W. Liu, *Microsyst. Technol.* **22**, 871 (2016)
38. B. Erdem, R.A. Hunsicker, G.W. Simmons, E.D. Sudol, V.L. Dimonie, M.S. El-Aasser, *Langmuir* **17**, 2664 (2001)

39. S. Kelly, F.H. Pollak, M. Tomkiewicz, J. Phys. Chem. B **101**, 2730 (1997)
40. X. Xue, W. Ji, Z. Mao, H. Mao, Y. Wang, X. Wang, W. Ruan, B. Zhao, J.R. Lombardi, J. Phys. Chem. C **116**, 8792 (2012)
41. L. Meng, C. Li, M.P. dos Santos, J. Inorg. Organomet. Polym. Mater. **21**, 770 (2011)
42. J. Ungula, B.F. Dejene, H.C. Swart, Results Phys. **7**, 2022 (2017)
43. M.A. Mansoor, N.M. Huang, V. McKee, T.A.N. Peiris, K.G.U. Wijayantha, Z. Arifin, M. Misran, M. Mazhar, Sol. Energy Mater. Sol. Cells **137**, 258 (2015)
44. M.A. Mansoor, M. Mazhar, A. Pandikumar, H. Khaledi, H. Nay Ming, Z. Arifin, Int. J. Hydrogen Energy **41**, 9267 (2016)
45. X. Zheng, S. Shen, F. Ren, G. Cai, Z. Xing, Y. Liu, D. Iiu, G. Zhang, X. Xiao, W. Wu, C. Jiang, Int. J. Hydrogen Energy **40**, 5034 (2015)

Affiliations

Muhammad Adil Mansoor^{1,2}  · Farazila Binti Yusof¹ · Huang Nay-Ming³

✉ Muhammad Adil Mansoor
adil_mansoor85@yahoo.com

Farazila Binti Yusof
farazila@um.edu.my

Huang Nay-Ming
huangnayming@gmail.com

² Department of Chemistry, School of Natural Sciences,
National University of Sciences and Technology, NUST HQ,
Scholars Avenue, H-12, 44000 Islamabad, Pakistan

³ New Energy Science and Engineering Department,
University of Xiamen Malaysia, Jalan SunSuria, Bandar
SunSuria, Selangor Darul Ehsan, 43900 Sepang, Malaysia

¹ Advanced Manufacturing and Materials Processing (AMMP)
Centre, Faculty of Engineering, University of Malaya,
50603 Kuala Lumpur, Malaysia